1 **A novel calcium-concentrating compartment drives biofilm formation and**
2 **persistent infections**

3 Alona Keren-Paz[1*], Malena Cohen-Cymberknoh[2*], Dror Kolodkin-Gal[3*], Iris
4 Karunker[1*,] Simon Dersch[4], Sharon G. Wolf[5], Tsviya Olender[1], Elena
5 Kartvelishvily[5], Sergey Kapishnikov[5], Peninnah Green-Zelinger[1], Michal
6 Shteinberg[6], Gideon Zamir[3], Assaf Gal[7], Peter Graumann[4], Eitan Kerem[2**], and
7 Ilana Kolodkin-Gal[1**]

8 [1] Department of Molecular Genetics, Weizmann Institute of Science, Rehovot,
9 Israel

10 [2] Pediatric Pulmonary Unit, Hadassah-Hebrew University Medical Center,
11 Jerusalem, Israel

12 [3] Department of Experimental Surgery, Hadassah-Hebrew University Medical
13 Center, Jerusalem, Israel

14 [4] Centre for Synthetic Microbiology (SYNMIKRO), and Fachbereich Chemie,
15 Philipps-Universität Marburg, Marburg, Germany.

16 [5] Chemical Research Support, Weizmann Institute of Science, Rehovot, Israel

17 [6] Pulmonology Institute and CF Center, Carmel Medical Center, Haifa, Israel

18 [7] Department of Plant and Environmental Sciences, Weizmann Institute of
19 Science, Rehovot, Israel

20 *Equal Contribution

21 **Corresponding   authors: Ilana.kolodkin-gal@weizmann.ac.il;
22 EitanK@hadassah.org.il

23

24

25

26

27

28

29

30

31

32

33

34

35

36

1

Abstract

Bacterial biofilms produce a robust internal mineral layer, composed of calcite, which strengthens the colony and protects the residing bacteria from antibiotics. In this work, we provide evidence that the assembly of a functional mineralized macro-structure begins with mineral precipitation within a defined cellular compartment in a differentiated subpopulation of cells. Transcriptomic analysis of a model organism, *Bacillus subtilis,* revealed that calcium was essential for activation of the biofilm state, and highlighted the role of cellular metal homeostasis and carbon metabolism in biomineralization. The molecular mechanisms promoting calcite formation were conserved in pathogenic *Pseudomonas aeruginosa* biofilms, resulting in formation of calcite crystals tightly associated with bacterial cells in sputum samples collected from cystic fibrosis patients. Biomineralization inhibitors targeting calcium uptake and carbonate accumulation significantly reduced the damage inflicted by *P. aeruginosa* biofilms to lung tissues. Therefore, better understanding of the conserved molecular mechanisms promoting biofilm calcification can path the way to the development of novel classes of antibiotics to combat otherwise untreatable biofilm infections.

Main text

In nature bacteria form differentiated multicellular communities, known as **biofilms**. Bacterial biofilms are of extreme clinical importance, as they are associated with many persistent and chronic bacterial infections (*1*). For example, the commensal/aquatic bacterium *P. aeruginosa* can cause devastating chronic biofilm infections in immune compromised hosts, in patients with cystic fibrosis (CF), and on the surface of medical devices and burn wounds (*1*). Bacteria in a biofilm can be up to 1,000 times more resistant to antibiotics than planktonic (free-living) bacteria (*2*). The mechanisms supporting this phenotypic resistance, as well as those driving the transition from free-living single bacteria to a differentiated biofilm community are still poorly understood (*1, 3*).

To date, the ability of biofilm-forming bacteria to form complex architectures was attributed exclusively to their **organic** extracellular matrix (ECM). However, we and others have recently shown that microbial biofilms contain a robust internal mineral layer, composed of crystalline calcium carbonate (calcite) (*4-7*). Calcification associated with biofilms was also observed in clinical settings, such as catheters (*8*). While the role of bacterial cells as nucleation sites in environmental carbonate mineral formation is long-established (*9*), it is so far considered an unintentional by-product of bacterial metabolic activity, random and unregulated, and serving no particular function for the mineral-associated bacteria.

In this work, we provide evidence that the assembly of a functional mineralized macro-structure begins with mineral precipitation within a defined cellular compartment in a subpopulation of biofilm cells. We show that calcium-dependent transcriptional reprogramming is essential for biofilm development and promotes calcite formation. Our results indicate that biofilm mineralization is tightly regulated

2

and highly conserved developmental process. Moreover, we show that targeting biofilm-associated mineralization can combat pathogenic biofilms in clinical settings.

When a *B. subtilis* biofilm colony was visualized by scanning electron microscopy (SEM), we observed a highly mineralized subpopulation of cells (Figure 1A), tightly associated with mineral crystals. The crystals were consistent with calcite, as judged by backscatter mode and energy dispersive X-ray spectroscopy (EDX) (Figure 1B, Figure S1). 3D reconstructions of cryo-fixed bacteria with scanning transmitting electron tomography (CSTET(*10*)) (Figure 1C-D, Figure S2 and S3) revealed calcium-rich foci inside the cells, between the membrane and peptidoglycan. The appearance of these deposits was calcium dependent, and highly correlated with the emergence of complex structural patterns (Figure S4). While the mineral producing sub-population was small, it was enriched in the structured zones of the colony (Figure 1E). Next, we stained live biofilm cell with Calcein-AM – a dye that can be used for visualization of intracellular calcium in live cells(*11*). Gated-STED fluorescent microscopy revealed heterogeneity in cellular calcium levels within the biofilm colony (Figure 1F, inset), and the number of cells showing a strong Calcein-AM signal increased during biofilm development (Fig. 1F). In 6 day old biofilms, we observed that a small fraction of cells (2.6%, n=300 cells) displaying membrane-localized intracellular calcium foci (Figure 1G), comparable in their distribution and localization with calcium crystals identified by CSTET. We detected several such loci associated with the cell envelope from within the cytoplasm, embedded within the membrane itself, and closely associated with the cell from the outside – suggesting different stages of export (Figure 1H). Similar calcium crystals in close association with the outer membrane of bacterial cells were also observed by CSTET (Figure 1I).

Taken together, those observations suggest that the first critical step in the formation of calcite is the development of intracellular saturated calcium carbonate microenvironments. After the initial nucleation, the calcite crystal seems to be exported out of the bacterial cell, to further grow on organic ECM templates into a functional mineral macro-structure.

To better understand the cellular pathways mediating intracellular mineral formation, we analyzed the effect of calcium on gene expression of biofilm cells. We sequenced the transcriptome of biofilm colonies with and without excess calcium (Figure 2A and Supplementary File 1). First, we compared the transcriptome obtained in this study to a formerly published transcriptome of *B. subtilis* (*12*) (Figure 2B). The transcriptome of cells grown with excess calcium was similar to that of previously analyzed biofilm cells, regardless of the biofilm promoting medium used. On the other hand, the transcription profile of colonies grown without excess calcium was similar to that of planktonic cells experiencing nutrient starvation – but did not reflect the specific developmental processes activating during biofilm development, such as ECM production, repression of motility and sporulation (Figure 2C). Those findings highlight the central role of calcium as a general cue for transition from planktonic growth to biofilm state.

3

125 We identified two specific pathways directly linked to biomineralization that were
126 regulated by intracellular calcium (Figure 2D-E). Global changes in metal
127 homeostasis, such as inhibition of the PerR regulon, suggest the need for tight
128 control of intracellular metal levels during mineral formation. Members of IolR
129 regulon catabolize myo-inositol, with CO_2 released as a byproduct. The inhibition
130 of their expression is consistent with the need for regulation of the location and
131 timing of carbonate accumulation . Consistently with their regulatory role, the
132 deletion of both *iolR* and *perR* caused defects in biofilm development, diminishing
133 and distorting the normally symmetric 3D architecture of the colonies (Figure 2F).
134 Finally, deletion of *cueR*, encoding a putative transcriptional regulator of at least
135 one P-type ATPase, lead to a formation of a completely flat colony (Figure 2F) –
136 suggesting the need for control of intracellular cation levels for the formation of
137 colony architecture. Likewise, chemical inhibition of P-type ATPases with sodium
138 metavanadate (SMV)(*13*) compromised biofilm morphology, similarly to the effect
139 of a known biomineralization inhibitor acetohydroxamic acid (AHA, urease inhibitor
140 (*7*)) (Figure 2G). Those morphological defects were not due to inhibition of
141 planktonic growth, which was similar between the wild type and the mutant strains
142 (Figure 2H). Taken together, those results confirm the involvement of specific
143 regulated cellular pathways for biofilm mineralization.

144 We have previously reported the seeming conservation of biofilm biomineralization
145 in the bacterial kingdom (*4*), and thus we set to see whether the insights gained by
146 studying the model bacterium *B. subtilis* can be relevant to clinical practice.
147 Respiratory infection with *P. aeruginosa* is a leading cause of morbidity and
148 mortality in patients with CF (*14*). Once chronic infection with *P. aeruginosa* is
149 established, it is almost impossible to eradicate (*15*). Calcification was recently
150 observed in *P. aeruginosa* biofilms *in vitro* (*6*), although the biological mechanism
151 of mineral formation remained to be determined. Visualizing biofilm colonies using
152 microCT-Xray demonstrated co-localization of complex 3D structures in *P.
153 aeruginosa* biofilm with spatially organized mineral (Figure 3A). Those structures
154 were abolished by cation chelator EDTA and restored by addition on excess
155 calcium (Figure 3B). Consistent with the evolutionary conserved nature of the
156 cellular pathways of biomineralization (Figure 3C), chemical inhibitors of cellular
157 carbonate production and inhibitor of calcium uptake interfered with *P. aeruginosa*
158 biofilm formation (Figure 3D, 3F), and abolished the mineral macrostructures
159 (Figure 3E). This effect could not be explained by inhibition of planktonic growth,
160 which as mostly unaffected (Figure 3F).

161 We then examined whether calcite formation by *P. aeruginosa* could be also
162 observed in clinical settings. FTIR analysis of sputum samples collected from CF
163 patients chronically infected with *P. aeruginosa* identified multiple samples
164 containing calcite (Figure 3G). Moreover, we were able to visualize mineral crystals
165 tightly associated with bacterial cells in the sputum samples (Figure 3H).

166 As we have previously shown that mineral structures protect biofilm cells from
167 penetration of antibiotics (*7*), we examined whether calcification can be targeted
168 to combat persistent infection. Towards this goal, we developed a novel *ex vivo*
169 system, where mice lung tissues are harvested, cultured, and then infected with *P.

4

170 *aeruginosa* expressing GFP. Fluorescent microscopy revealed biofilms forming on
171 the tissue prior to its destruction (Figure 4A). Using this system, we tested the
172 effect of chemically blocking biomineralization during initial infection stages.
173 Urease inhibition prevented biofilm formation and rescued the lung tissue, without
174 reducing bacterial load (Figure 4B-C). Similar results were obtained with carbonic
175 anhydrase and calcium uptake inhibitors (Figure 4D and Figure S5). Preventing
176 calcification significantly reduced lung cell death (Figure 4E). Finally, while neither
177 biomineralization inhibitors nor quinolone antibiotics (a first-line antibiotic for
178 treating *P. aeruginosa* infections) could not effectively eradicate established
179 biofilms, the combination of both classes of drugs significantly increased the
180 sensitivity of biofilms to treatment (Figure 4F), consistent with the role of the
181 mineral in protecting the biofilm and confirming the potential importance of biofilm
182 biomineralization in clinical settings.

183 Our work suggests that it is time to reconsider the old definition of bacterial
184 associated mineralization as a passive, unintended byproduct of environmental
185 bacterial activity. Instead, we here provide evidences that it is a defined and
186 regulated developmental process, conferring clear benefits to the bacteria.
187 Understanding the molecular mechanisms that regulate mineralization can identify
188 numerous novel targets for antibiotics, and lead to development of novel classes
189 of drugs to combat biofilm infections - and thus is of enormous clinical significance.

190

References

192 1.   J. W. Costerton, P. S. Stewart, E. P. Greenberg, Bacterial biofilms: a common cause
193   of persistent infections. *Science* **284**, 1318-1322 (1999).
194 2.   J. D. Bryers, Medical biofilms. *Biotechnol Bioeng* **100**, 1-18 (2008).
195 3.   A. Erez, I. Kolodkin-Gal, From Prokaryotes to Cancer: Glutamine Flux in
196   Multicellular Units. *Trends Endocrinol Metab* **28**, 637-644 (2017).
197 4.   Y. Oppenheimer-Shaanan *et al.*, Spatio-temporal assembly of functional mineral
198   scaffolds within microbial biofilms. *NPJ Biofilms Microbiomes* **2**, 15031 (2016).
199 5.   X. Li *et al.*, Spatial patterns of carbonate biomineralization in biofilms. *Appl
200   Environ Microbiol* **81**, 7403-7410 (2015).
201 6.   X. Li *et al.*, In Situ Biomineralization and Particle Deposition Distinctively Mediate
202   Biofilm Susceptibility to Chlorine. *Appl Environ Microbiol* **82**, 2886-2892 (2016).
203 7.   A. Keren-Paz, V. Brumfeld, Y. Oppenheimer-Shaanan, I. Kolodkin-Gal, Micro-CT
204   X-ray imaging exposes structured diffusion barriers within biofilms. *NPJ biofilms
205   and microbiomes* **4**, 8 (2018).
206 8.   D. Stickler, N. Morris, M. C. Moreno, N. Sabbuba, Studies on the formation of
207   crystalline bacterial biofilms on urethral catheters. *Eur J Clin Microbiol Infect Dis*
208   **17**, 649-652 (1998).
209 9.   S. Douglas, T. J. Beveridge, Mineral formation by bacteria in natural microbial
210   communities. *Fems Microbiology Ecology* **26**, 79-88 (1998).
211 10.   S. G. Wolf, L. Houben, M. Elbaum, Cryo-scanning transmission electron
212   tomography of vitrified cells. *Nat Methods* **11**, 423-428 (2014).

5

213 11.   L. V. Hale, Y. F. Ma, R. F. Santerre, Semi-quantitative fluorescence analysis of
214   calcein binding as a measurement of in vitro mineralization. *Calcified Tissue Int*
215   **67**, 80-84 (2000).
216 12.   P. Nicolas *et al.*, Condition-dependent transcriptome reveals high-level regulatory
217   architecture in Bacillus subtilis. *Science* **335**, 1103-1106 (2012).
218 13.   M. Guragain, D. L. Lenaburg, F. S. Moore, I. Reutlinger, M. A. Patrauchan,
219   Calcium homeostasis in Pseudomonas aeruginosa requires multiple transporters
220   and modulates swarming motility. *Cell Calcium* **54**, 350-361 (2013).
221 14.   S. S. Yoon, D. J. Hassett, Chronic Pseudomonas aeruginosa infection in cystic
222   fibrosis airway disease: metabolic changes that unravel novel drug targets. *Expert*
223   *review of anti-infective therapy* **2**, 611-623 (2004).
224 15.   M. Cohen-Cymberknoh *et al.*, Eradication failure of newly acquired Pseudomonas
225   aeruginosa isolates in cystic fibrosis. *Journal of cystic fibrosis : official journal of*
226   *the European Cystic Fibrosis Society*, (2016).
227 16.   G. A. O'Toole, Microtiter dish biofilm formation assay. *J Vis Exp*, (2011).
228 17.   T. Bucher, E. Kartvelishvily, I. Kolodkin-Gal, Methodologies for Studying B.
229   subtilis Biofilms as a Model for Characterizing Small Molecule Biofilm Inhibitors.
230   *J Vis Exp*, (2016).

231

232

233 **Figure Legends:**

234

235 **Figure 1:**

236 *B. subtilis* NCIB 3610 was inoculated on solid biofilm inducing medium
237 supplemented with 0.25% calcium acetate (v/v), and incubated at 30°C for 3 or 6
238 days.

239 A. Scanning Electron Microscopy (SEM) image obtained using secondary
240   electron mode. Shown is the surface of a 6 day-old biofilm. Rhombohedral
241   calcite structures accompanied by calcified cells are clearly visible.
242   Magnification – X25000, scale bar – 1 µm.

243 B. Backscattered mode SEM image of the area shown in (A), and EDX spectra of
244   indicated areas used to confirm specific accumulation of calcium carbonate.
245   CA – calcium rich area; Cnt – control area.

246 C. A 30-nm thick virtual slice through a CSTET 3D reconstruction of bacterial cells.
247   Inset - EDX spectrum used to identify calcium accumulation. Arrows indicate
248   calcium deposits between the membrane and the peptidoglycan. Scale bar =
249   400 nm.

250 D. Volume rendering (orange) and a single orthoslice (greyscale) through the
251   center of the volume, from a 3D CSTET reconstruction. The minerals are
252   artificially colored (blue).

253 E. Quantification of different subpopulations within either a structured zone of the
254   biofilm colony, grown as in A, or an entire colony. CryoSTEM multi-image
255   montaged maps with large fields of view were manually analyzed for cells with
256   mineral foci.

6

F. Mean fluorescence intensities (A.U.x10^4) of bacterial cells (n=150) isolated from biofilm colonies (day 3 and 6), stained with Calcein-AM – a calcium-binding dye that only becomes fluorescent after hydrolysis by cellular esterases. Inset – a representative image of cells isolated from a 6 days old biofilm. Green – calceinAM, red – NileRed membrane stain, gray – DIC. Scale bar: 2 μm.

G. and H. G-STED images of bacterial cells, isolated from biofilm colonies. Green – calceinAM, red – NileRed membrane stain, gray – DIC. Scale bar: 2 μm.

I. 30-nm thick virtual slice through a CSTET 3D reconstruction. Arrows indicate calcium-rich foci associated with a membrane from the outside of the cell.

Figure 2:

A. Transcription profile of *B. subtilis* NCIB 3610 biofilm colonies grown for 1, 3 and 6 days on a biofilm-inducing B4-Ca agar, with and without added excess calcium. A heatmap with all differentially expressed genes (n = 876), scaled to the mean expression level of each gene. The map is ordered by age of biofilm colonies, as shown by the left colored bar, where green are genes that are differentially expressed in days 1-3, and day 6; purple genes that are differentially expressed in days 1-3 and yellow genes that are differentially expressed in day 6.

B. The top 20 conditions from the study of Nicolas *et al* (9), showing the highest similarity to the transcriptome of 6-day old biofilm colonies grown without or with calcium (top panel and bottom panel, respectively).

C-D. Volcano-plot depicting calcium-dependent changes in expression of genes. Genes belonging to the indicated functional categories, as determined by DAVID analysis, are highlighted.

E. Calcium-dependent change in gene expression of genes highlighted in D, expressed as log 2 fold change.

F. Top-down images of biofilm colonies of wild-type *B. subtilis* strain and the indicated mutant derivatives, grown on solid biofilm-inducing medium B4, with added excess calcium, for 3 days at 30°C.

G. Top-down images of biofilm colonies of wild-type *B. subtilis* grown for 3 days at 30°C on solid B4 biofilm-inducing medium, with added excess calcium, and supplemented with indicated inhibitors (0.1 mg/ml SMV, 2.5 mg/ml AHA).

H. Planktonic growth assays. Wild type and the indicated mutant derivatives were grown at 30°C with shaking in liquid B4 medium supplemented with calcium, and growth was monitored by measuring OD$_{600}$ in a microplate reader every 30 min. Results are averages of nine wells, bars represent standard deviations. A representative experiment out of at least 3 independent experiments is shown.

Figure 3:

7

299   A. Top-down images of biofilm colonies of wild type *P. aeruginosa* PA14 colonies
300   grown for 3 days at 23°C on solid TB medium. Phase and microCT-X-ray
301   images are shown. In the X-Ray images, the bright contrast indicates the
302   location of dense mineral, while the organic matter appears dark in the image.
303   Scale bar – 2 mm.

304   B. Top-down images of biofilm colonies of wild type *P. aeruginosa* PA14 colonies
305   grown for 3 days at 23°C on solid TB medium containing 1 mg/ml EDTA, either
306   with or without the addition of 700 mM $CaCl_2$.

307   C. A schematic representation of the chemical reaction leading to calcium
308   carbonate production, with the inhibitors used in this study indicated in
309   parenthesis next to the step they inhibit. Scale bar – 2 mm.

310   D. Top-down images of biofilm colonies of wild type *P. aeruginosa* PA14 colonies
311   grown for 3 days at 23°C on solid TB medium containing the indicated inhibitors
312   as follows: 1.5 mg/ml DTNB, 1.75 mg/ml AHA, 2.5 mg/ml Diamox and 0.01
313   mg/ml SMV.

314   E. MicroCT-XRay image of a wild type *P. aeruginosa* PAO14 colony grown for 3
315   days at 23°C on solid TB medium containing SMV (0.01 mg/ml). The absence
316   of visible bright areas indicates lack of dense mineral.

317   F. Crystal violet assay for biofilm formation (*16*). Wild type *P. aeruginosa* PA14
318   biofilms were grown with indicated inhibitors for 24 h in TB medium. Results
319   are averages and standard deviation of three independent experiments. P
320   values, as determined by student's t-test are indicated (* pVal <0.01, ** pVal
321   <0.001, when compared to the untreated control).

322   G. Planktonic growth assays. *P. aeruginosa* PA14 was grown at 37°C with shaking
323   in liquid TB medium, supplemented with: 1.5 mg/ml DTNB, 1.75 mg/ml AHA,
324   2.5 mg/ml Diamox and 0.01, 0.05 and 0.01 mg/ml SMV. Growth was monitored
325   by measuring OD_{600} in a microplate reader every 30 min. Results are averages
326   of six wells, bars represent standard deviations. A representative experiment
327   out of at least 3 independent experiments is shown.

328   H. FTIR spectra of bleached sputum samples of six individual *P. aeruginosa*
329   positive CF patients. Arrows indicate vibrations characteristic of calcite.

330   I. SEM images of a sputum sample from *P. aeruginosa* positive CF patient. White
331   arrows indicate calcite crystals and a yellow arrow indicated highly mineralizes
332   bacterial cells.

333

Figure 4:

335   A. Fresh lungs were harvested from one month old mice. Using a biopsy
336   punch, the tissue was divided into 3 mm circular pieces and transferred to
337   a 24 well plate (4-5 explants/well) with DMEM containing carbenicillin 100
338   µg/ml. To each respective well, either DMEM (control) or *P. aeruginosa*
339   PA14 expressing GFP (green) were added. The plates were incubated at
340   37ºC for 2 days, fixed and imbedded in cryosection compound. The
341   samples were cut into 10 micron slices, stained with DAPI and visualized

8

with confocal microscopy (magnification x40). Green – GFP-expressing bacteria, blue – lung cell nuclei stained with DAPI, red – false coloring of the lung tissue.

B. Lungs were harvested from one month old mice and prepared as indicated in (A). Tissue slices were incubated in DMEM 5% FCS, either with or without urease inhibitor AHA at indicated concentrations. To each sample, either *P. aeruginosa* or fresh medium (control) was added. Samples were incubated at 37⁰C for 2 days, fixed and imbedded in cryosection compound. The samples were cut into 10 micron slices, stained with DAPI and visualized under fluorescent microscopy (magnification x20). Blue - lung cell nuclei stained with DAPI, green – GFP expressing *P. aeruginosa* attached to the lung.

C. Samples were prepared as in (B), but imbedded in paraffin, cut into 7 micron slices, stained with H&E and visualized under light microscopy (magnification x40).

D. Samples were treated with different biomineralization inhibitors, as indicated, and prepared as in (C).

E. To quantify the effect of the treatments on lung viability, ImageJ 1.51g software was used to automatically count lung cell nuclei in 4 randomly chosen fields for each treatment. P values, as determined by student's t-test are indicated (** pVal <0.001).

F. The effect of biomineralization inhibition on the resistance of established biofilms to antibiotics. *P. aeruginosa* PA14 biofilms were grown for 72 h on solid TB medium and treated as previously described (*17*). The colonies were physically divided into equal parts, harvested, and half was treated for 2 h as indicated (CIP – Ciprofloxacin, 3 mg/ml, GC – gentamycin, 10 mg/ml, AHA – 2.5 mg/ml AHA, DTNB – 2 mg/ml DTNB). Viability is expressed as the ratio of CFU between the treated and the untreated parts of a colony. Results are averages and standard deviation of three independent experiments performed in duplicates. P values, as determined by student's t-test are indicated (** pVal <0.001).
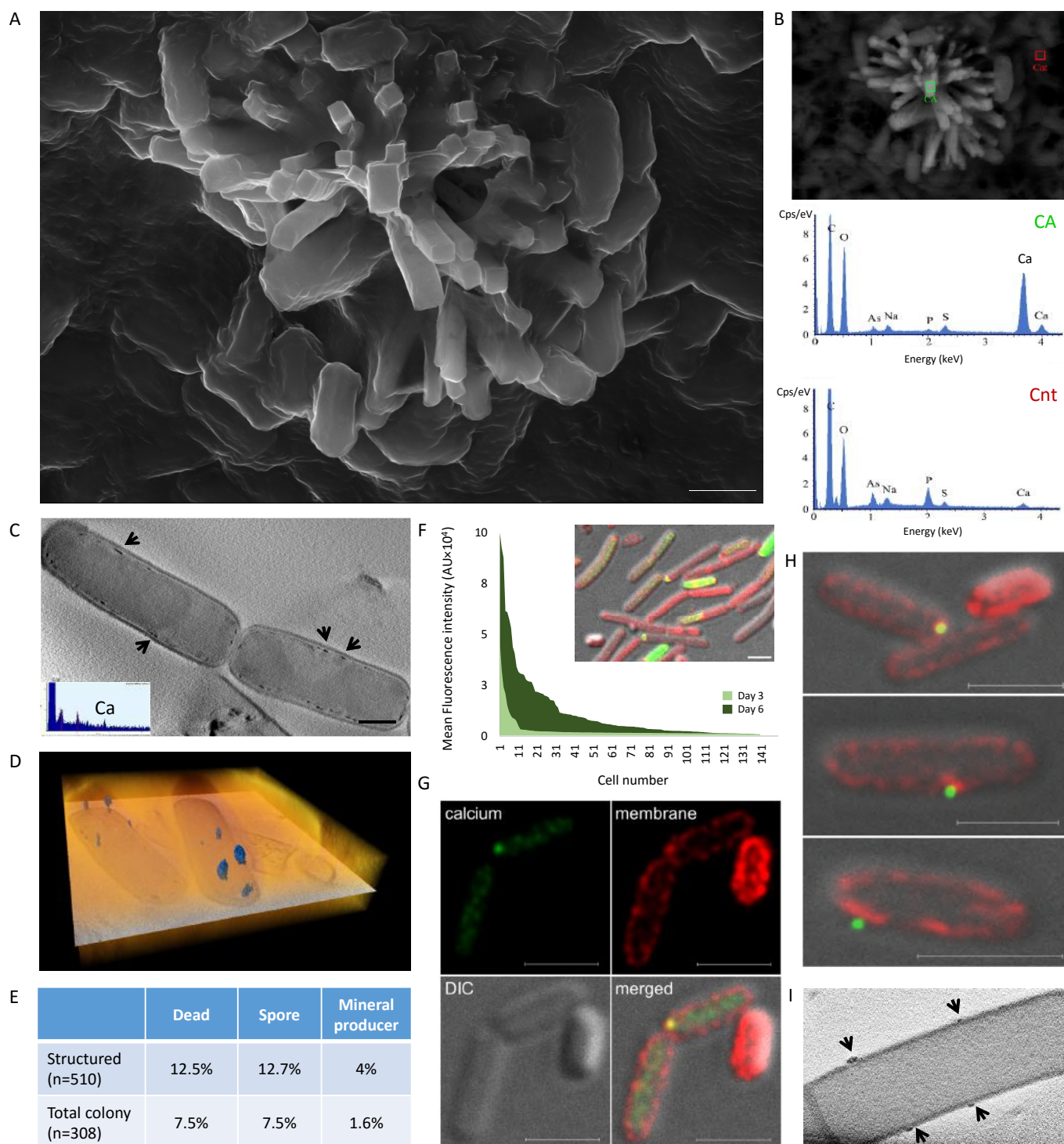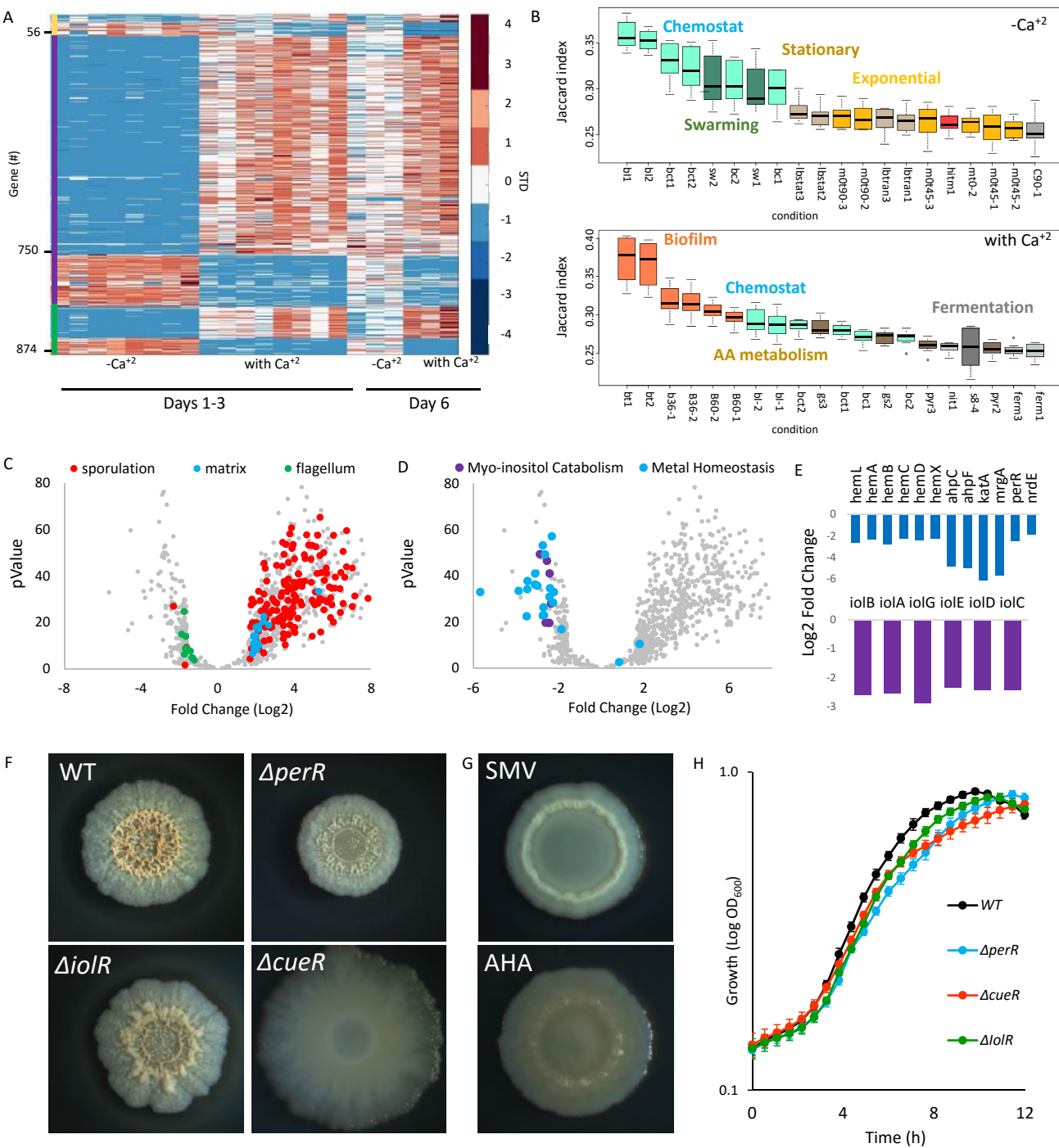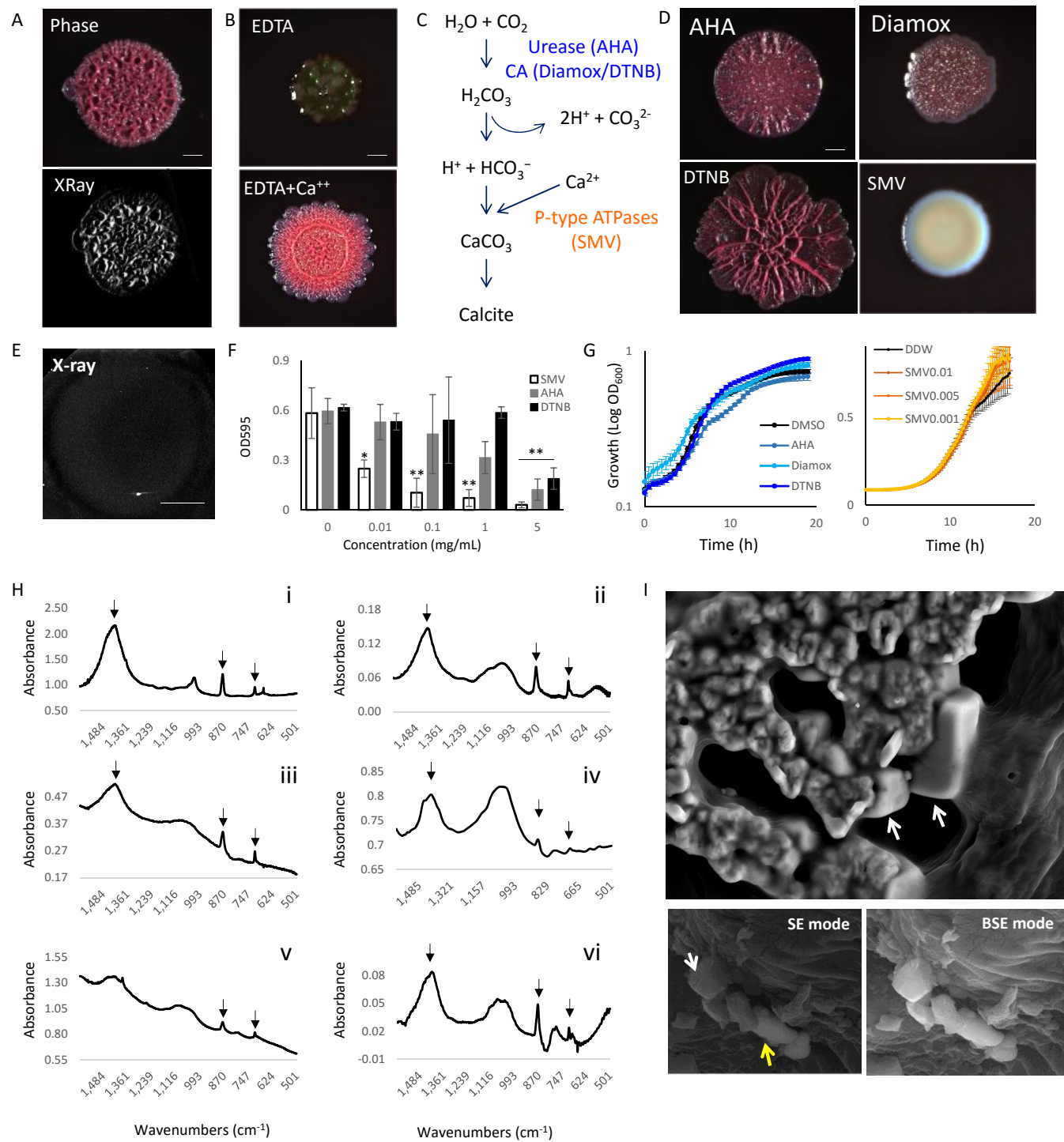
9

Figure 1

Figure 2
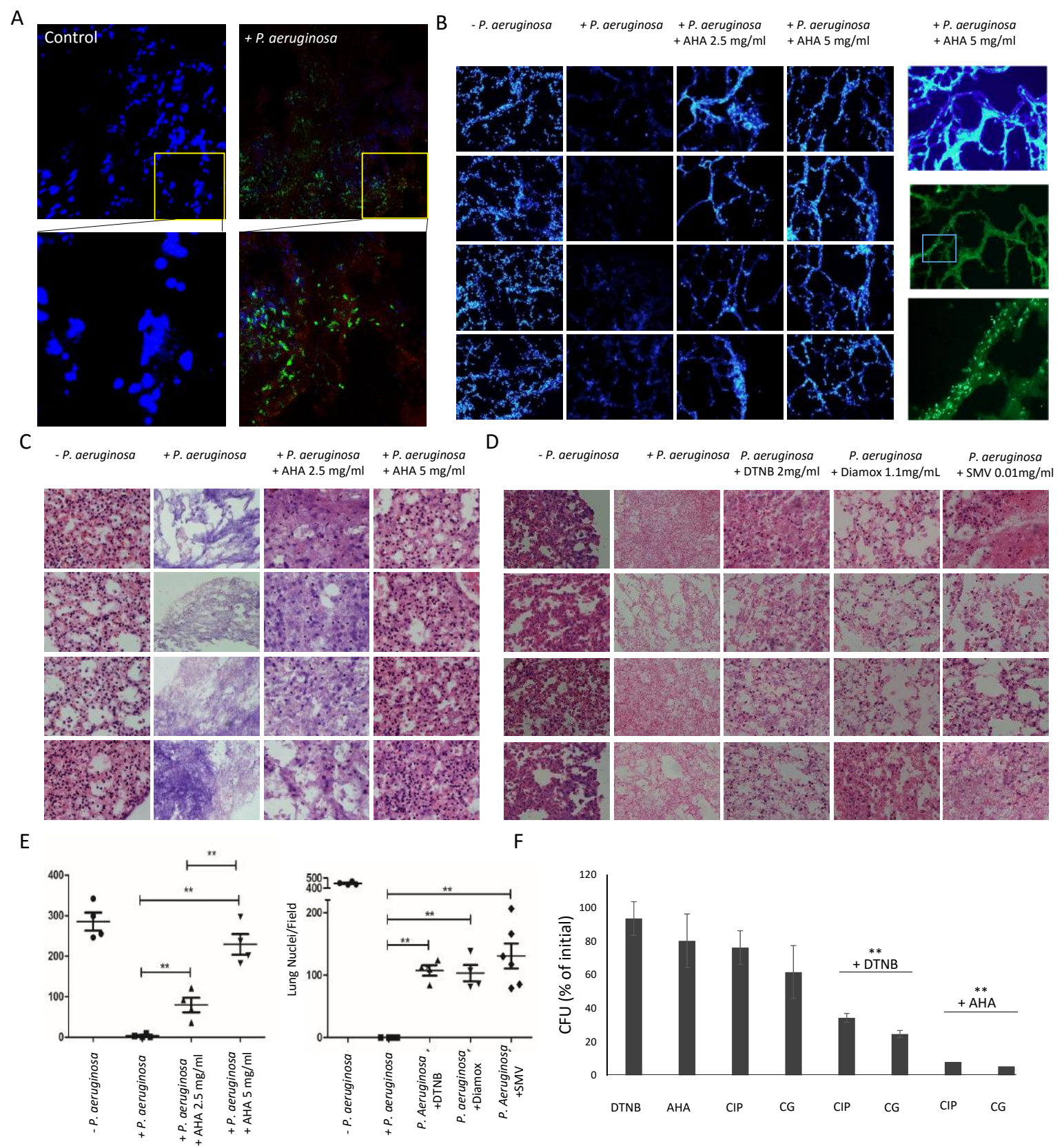
Figure 3

Figure 4

A novel microbial compartment drives biofilm formation and persistent Infections

Supporting Information

Content

Supporting Materials and Methods

Supporting Figures

Supporting References

Supporting Files

Supporting Tables

Supporting Materials and Methods

Strains and media

All strains used in this work were derivatives from wild type *Bacillus subtilis* NCIB 3610 or *Pseudomonas aeruginosa strain PA14* . A list of strains used in this study can be found in Sup. Table 1. Deletions were generated transforming *B. subtilis* NCIB 3610 with genomic DNA isolated from *B. subtilis* 168 deletion library {Koo, 2017 #6} (Addgene, Cat#1000000115) , and verified by PCR*.*

B. subtilis biofilms were grown on B4 biofilm-promoting solid medium (0.4% yeast extract, 0.5% glucose, and 1.5% agar) (*1*) supplemented with calcium acetate at 0.025% v/v, incubated at 30°C in a sealed box for enriched CO_2 environment achieved by using the candle jar method (*2*).

P. aeruginosa biofilms were grown on TB medium, as described previously (*3*).

Patient's samples: Sputum was collected from adult patients as published previously (*4*) and stored in 4⁰C degrees to allow microscopy. All patients positive for calcite were carrying chronic *pseudomonas* infections. Specific patient information can be found in Sup. Table 2. The patients samples were collected under Helskinki approval to Prof. Eitan Keren 0435-17-HMO.

Scanning electron microscopy and EDX

Biofilm colonies were grown for 1, 3, 6, 10 and 15 days at 30°C on biofilm-promoting B4 solid medium, with or without calcium. The colonies were fixed

overnight at 4°C with 2% glutaraldehyde, 3% paraformaldehyde, 0.1 M sodium cacodylate (pH 7.4) and 5 mM $CaCl_2$, dehydrated and dried as described by Bucher *et al.*) (*5, 6*). Clinical samples were first partially or completely bleached to remove the organic material by 1 hour of incubation in either 3% or 6% sodium hypochlorite, respectively. The insoluble material was collected, washed three times in PBS, three times in acetone and air-dried for 16 hours.

Mounted samples were coated with 15 nm thick carbon layer in carbon coater (EDWARDS). The imaging by secondary electron (SE) or back scattered electron (BSE) detectors and the Energy Dispersive X-ray Spectroscopy (EDS, Bruker) were performed using Carl Zeiss Ultra 55 or Supra scanning electron microscopes.

Cryo-STEM analysis

Bacterial colonies grown as described were suspended in PBS buffer. Quantifoil TEM grids were glow-discharged with an Evactron Combi-Clean glow-discharge device, and 5 microliters of suspended cells were deposited onto the glow-discharged grids. Ten nm-diameter gold fiducials (*7*) were applied before blotting and vitrification using a Leica EM-GP automated plunging device (Leica).

Vitrified samples were observed with a Tecnai F20 S/TEM instrument (Thermo Fisher Scientific) at 200 kV, with Gatan 805 brightfield and Fischione HAADF detectors. Microscope conditions: extraction voltage = 4300 V, gun lens = 3 or 6, and spot size = 5 or 6 with 10 micrometer condenser apertures, yielding probe diameters of 1-2 nm and semi-convergence angles of ~ 1.3- 2.7 mrad. Images of

2048 X 2048 pixels were recorded with probe dwell times of 8-18 microseconds. Spatial sampling was set between 1 and 4 nm/pixel. Electron doses were 1–3 electrons/A^2 per dwell spot. Single-axis tilt series were recorded using SerialEM (*8*). EDX was performed in STEM mode on vitrified cell samples with the same electron microscope set-up as used for STEM imaging, using a liquid N_2 cooled Si(Li) detector (EDAX). Vitrified grids were imaged on a Talos Arctica (Thermo Fisher Scientific) microscope in STEM mode, and mapped at intermediate magnifications (10-13k) using SerialEM software to obtain large fields of view for quantification used in Fig. 1E.

Tomography reconstructions and visualization

The CSTET tomographic tilt series were aligned using fiducial markers and reconstructed using weighted back projection (*9*) (as implemented in the IMOD software suite (*8*). Reconstructions are displayed after non-linear anisotropic diffusion filtering within IMOD. Segmentation and volume rendering were performed using Amira 6.3 (FEI Visualization Sciences Group).

STED image acquisition

Cells were isolated from 3-6 day old biofilm colonies and stained with Calcein-AM (20 µM) and NileRed (100 µg/ml). Immediately after the staining procedure, the cells were mounted on a coverslip and immobilized by an agarose pad (1% agarose, S750 minimal media). STED microscopy was performed using a Leica

SP8 confocal microscope with a 100x oil immersion objective (NA: 1.4). A 552 nm laser line was used for confocal detection of NileRed, a 494 nm excitation laser and a 592 nm depletion laser were used for G-STED detection of Calcein-AM. Channels were acquired with 200 Hz (4 x line averaging) and the appropriately set HyD hybrid detectors. Images processing was performed using Leica LAS X and the deconvolution of the respective channels was performed using the Huygens algorithm.

RNA extraction and library preparation

Biofilm colonies were grown on biofilm-promoting B4 solid medium with and without calcium for 1, 2, 3 and 6 days. Three independent experiments were conducted, with three colonies from each treatment combined for RNA extraction in each experiment. The samples were frozen in liquid nitrogen and stored until extraction. Frozen bacterial pellets were lysed using the Fastprep homogenizer (MP Biomedicals) and RNA was extracted with the FastRNA PROT blue kit (MP Biomedicals, 116025050) according to the manufacturer's instructions. RNA levels and integrity were determined by Qubit RNA BR Assay Kit (Life Technologies, Q10210) and TapeStation, respectively. All RNA samples were treated with TURBO DNase (Life Technologies, AM2238).

A total of 5 ug RNA from each sample was subjected to rRNA depletion using the Illumina Ribo-Zero rRNA Removal Kit (Bacteria, MRZB12424), according to the manufacturers' protocols. RNA quantity and quality post-depletion was assessed as described above. RNA-seq libraries were contracted with NEBNext® Ultra™

Directional RNA Library Prep Kit (NEB, E7420) according to the manufacturer's instructions. Libraries concentrations and sizes were evaluated as above, and were sequenced as multiplex indexes in one lane using the Illumina HighSeq2500 platform.

RNAseq processing

Reads were trimmed from their adapter with cutadapt and aligned to the *B. subtilis* genome (subsp. *subtilis* str. NCIB 3610, NZ_CM000488.1) with Bowtie2 version 2.3.4.1 (*10*). The number of uniquely mapped reads per gene was calculated with HT-seq (*11*). Normalization and testing for differential expression was performed with DESeq2 v1.16. A gene was considered to be differentially expressed using the following criteria: normalized mean read count ≥ 30, fold change ≥ 3, and adjusted p value < 0.05. First, we tested for differential expression between samples grown with and without calcium separately for each time point; however, since the results for days 1, 2 and 3 were the same we joined days 1-3. The crude read count, normalized read count, and the result of the differentially expression tests are available in Sup. File 1.

Comparison between growth conditions

We compared our RNAseq expression data to publically available 269 transcriptomes representing 269 different growth conditions (*12*). Because that study used microarray platform and not RNAseq, the comparison was performed

using the top 10% genes with the highest expression level of every condition and every replicate (383 genes per sample). We than used Jaccard index to measure the overlap between the conditions of the two platforms (i.e. the current study and (*12*). Prior to the analysis, we removed 152 genes that appear among the top 10% in more than 80% of the conditions.

Regulon analysis

To analyze the data by regulons, we downloaded from Subtiwiki (*13*) the complete the list of the *B. subtilis* regulons and their associated genes. For every regulon, we calculated the average expression of the differentially expressed genes that are associated with the regulon (for days 1-3). We note that a gene can be associated with more than one regulon. Out of 215 Subtiwiki regulons, 83 were found to contain differentially expressed genes (Sup. File 1).

Phase microscopy

Biofilm colonies were observed using a Nikon D3 camera or a Stereo Discovery V20" microscope (Tochigi, Japan) with objectives Plan Apo S × 0.5 FWD 134 mm or Apo S × 1.0 FWD 60 mm (Zeiss, Goettingen, Germany) attached to Axiocam camera, as required. Data were captured using Axiovision suite software (Zeiss).

Planktonic growth assays

All strains were grown from a single colony isolated over LB plates to a mid-logarithmic phase of growth (4 h at 37°C with shaking). Cells were diluted 1:100 in 150 µl liquid B4 medium with and without calcium in 96-well microplate (Thermo Scientific). Cells were grown at 30°C or 37°C for 14–20 h in a microplate reader (Synergy 2, BioTek), and the optical density at 600 nm (OD_{600}) was measured every 15 min. Three independent experiments were conducted, with three technical repeats per plate. Crystal-violet biofilm assay was carried out as previously described (*14*). CFU assay was carried out as previously described (*5*).

Micro-CT X-ray analysis

Images of indicated magnification were taken using a Zeiss micro XCT 400 instrument (Pleasanton, CA, USA). Tomography was carried out using a micro-focused source set at 20 kV and 100 µA. 1200 separate 2D images were taken with a pixel size of 0.87 mm over 1800, exposure time of 30 sec. Image analysis was carried out with Avizo software (VSG, Hillsboro, OR, USA).

FTIR spectrophotometer analysis

FTIR spectra of the bleached samples were acquired in KBr pellets by using a NICOLET iS5 spectrometer (Thermo Scientific, Pittsburgh, PA, USA). The samples were homogenised in an agate mortar and pestle with about 40 mg of KBr, and pressed into a 7 mm pellet using a manual hydraulic press (Specac, Orpington, UK). Infrared spectra were obtained at 4 cm−1 resolution for 32 scans.

Ex vivo lung infection system

Animal work was carried out under ethical approval MD-16-15035-1. Lungs were harvested from 2 mice (one month old) and placed in petri dishes containing DMEM 5% FCS. The tissue was divided into circular pieces 3 mm in diameter with a biopsy punch and transferred to a 24 well plate (4-5 explants/well) with 450 µl DMEM containing carbenicillin 100 µg/ml (Sigma-Aldrich) and 0, 2.5, or 5 mg/ml AHA. To each respective well, we added either 50 µl DMEM (control) or *P. aeruginosa* (which was pretreated with 0, 2.5, or 5 mg/ml AHA and diluted within DMEM to attain OD_{600} 0.373) – with three technical repeats for each condition. The plates were incubated at 37ºC for ~2 days (52 hours) and washed twice with PBS, fixed with PFA 4% for 10 minutes, and imbedded in either cryosection (OCT) compound or paraffin. Paraffin samples were cut into 7 micron slices and stained with H&E; whereas cryosections were cut into 10 micron slices and placed on superfrost plus slides.
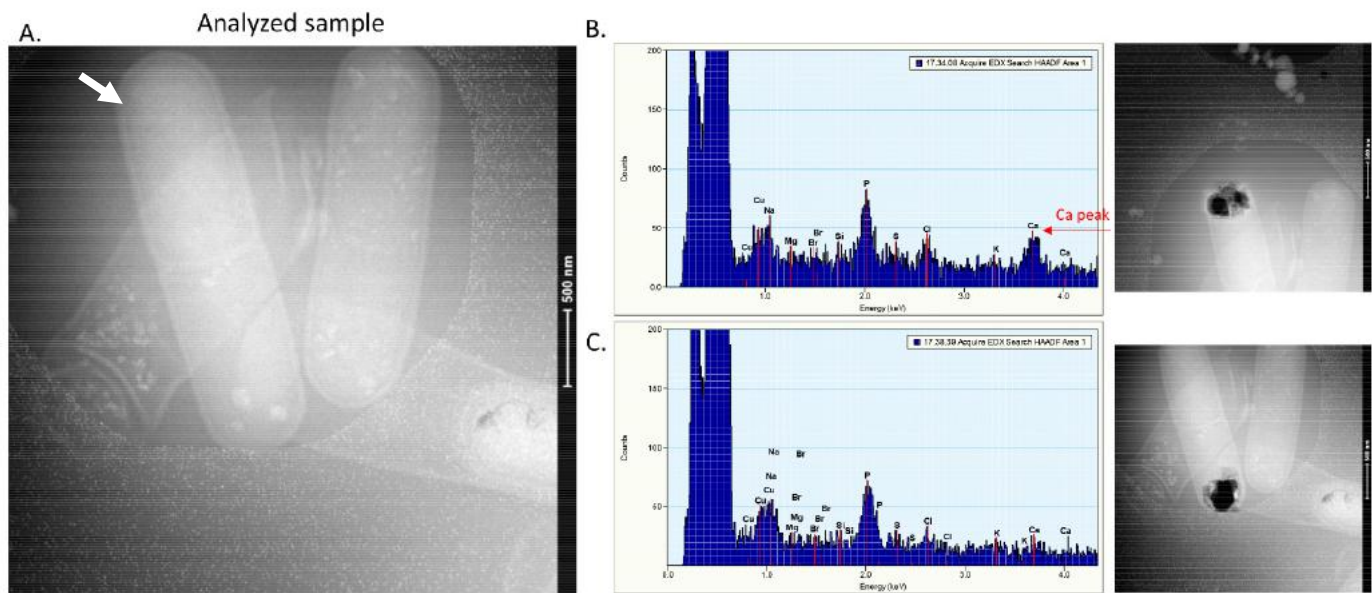
Supporting figures
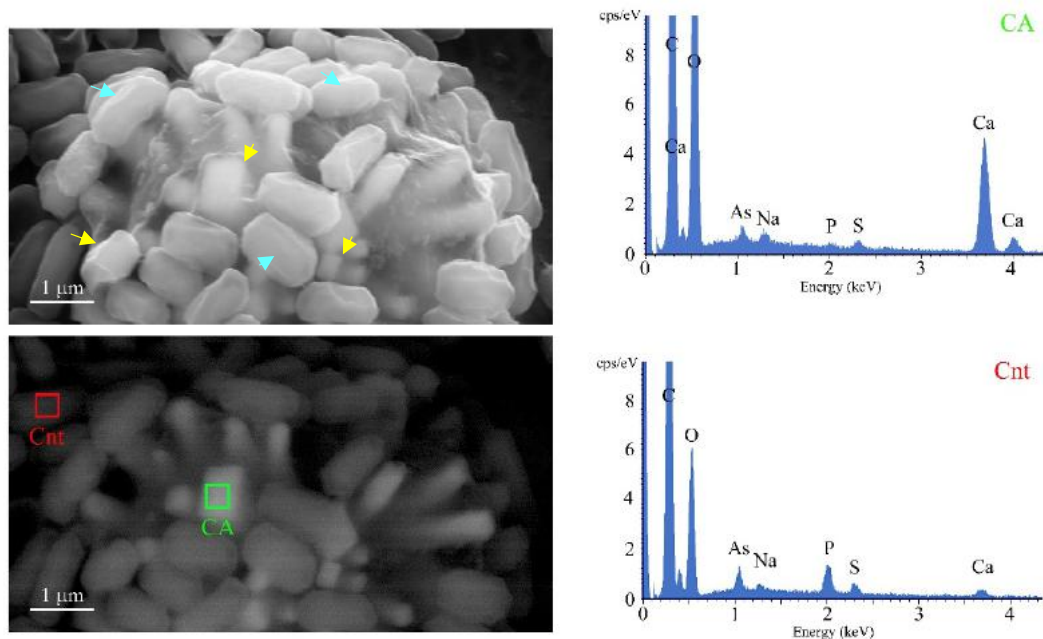
Supporting Figure 1: Scanning Electron Microscopy (SEM) image of biofilms (10 days). Shown are the surface of the biofilm and rhombohedral mineral structures in secondary (top panel) and backscattering (bottom panel) modes. The minerals (indicated by blue arrows) within the biofilms are accompanied by mineralized cells (indicated by yellow arrows). Indicated areas were analyzed by EDX to confirm the specific accumulation of calcium carbonate. CA – calcium-rich area, Cnt – control area.
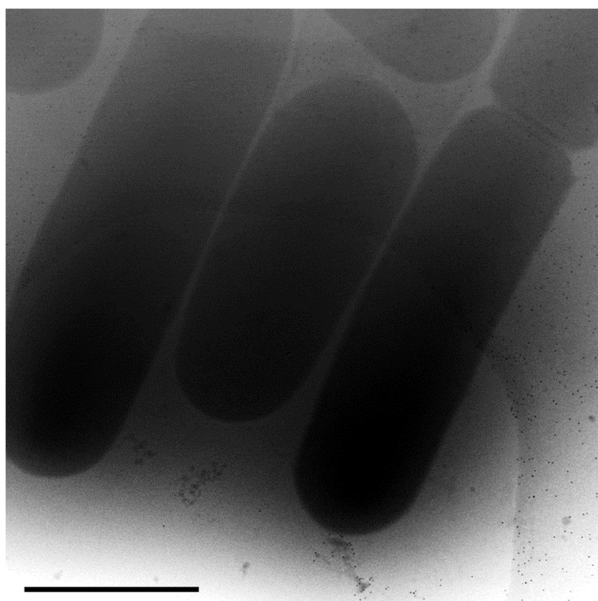
Supporting Figure 2. Cryo-STEM darkfield images of representative biofilm cells.

Cells grown without calcium appear to be uniform. Scale bar 1 μm.

Supporting Figure 3.   A. Darkfield STEM image of representative biofilm cells from a subpopulation showing deposits (10 days with calcium). The cell used for EDX analysis in panel (B) is indicated by the white arrow. B. EDX analysis of a calcium deposit (top) versus control area (bottom) confirms that the calcium is localized to the deposit. Cadmium originated from the grid for both areas.

+ Ca   - Ca
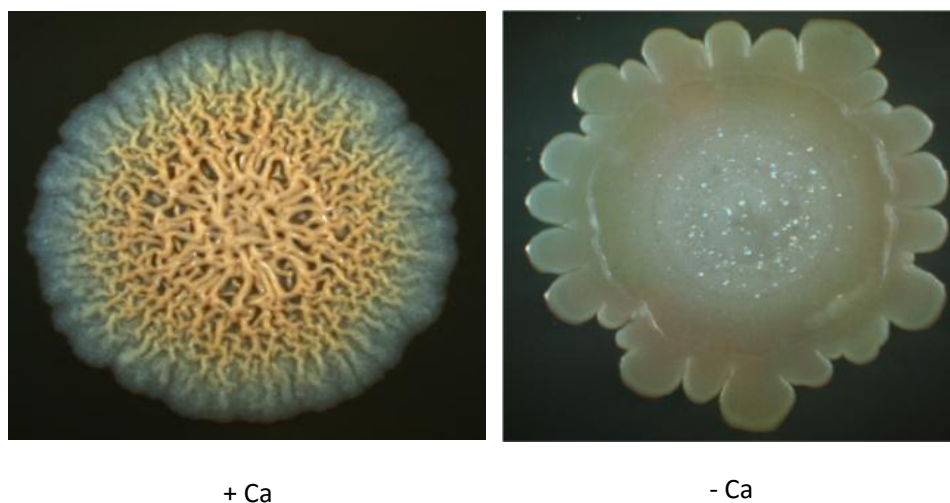
Supporting Figure 4. Top-down images of biofilm colonies grown on solid biofilm-inducing medium B4 for 6 days at 30°C in absence or presence of calcium as indicated.

DTNB   Diamox
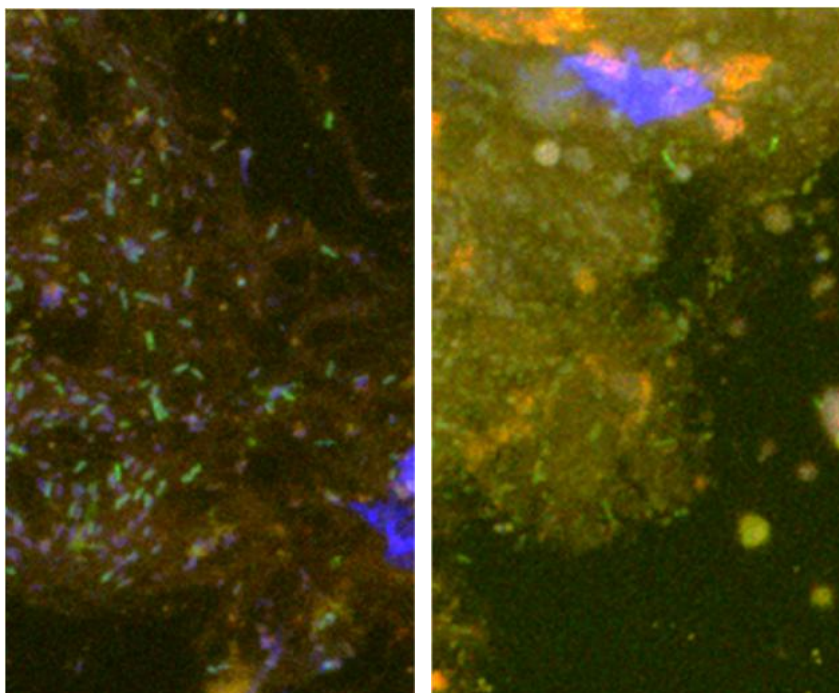
Supporting Figure 5. Confocal images of lung tissue grown as in Figure 4C, indicating the presence of microbial cells (GFP-expressing *P. aeruginosa* cells, green), but no viable lung cells (the absence of intact DAPI-stained nuclei, blue). Orange/red – false coloring o the tissue.

Supporting References:

1. C. Barabesi *et al.*, Bacillus subtilis gene cluster involved in calcium carbonate biomineralization. *J Bacteriol* **189**, 228-235 (2007).
2. Y. Oppenheimer-Shaanan *et al.*, Spatio-temporal assembly of functional mineral scaffolds within microbial biofilms. *NPJ Biofilms Microbiomes* **2**, 15031 (2016).
3. L. E. Dietrich *et al.*, Bacterial community morphogenesis is intimately linked to the intracellular redox state. *J Bacteriol* **195**, 1371-1380 (2013).
4. N. L. Schiller, R. L. Millard, Pseudomonas-infected cystic fibrosis patient sputum inhibits the bactericidal activity of normal human serum. *Pediatr Res* **17**, 747-752 (1983).
5. T. Bucher, E. Kartvelishvily, I. Kolodkin-Gal, Methodologies for Studying B. subtilis Biofilms as a Model for Characterizing Small Molecule Biofilm Inhibitors. *Journal of visualized experiments : JoVE*, (2016).
6. T. Bucher, Y. Oppenheimer-Shaanan, A. Savidor, Z. Bloom-Ackermann, I. Kolodkin-Gal, Disturbance of the bacterial cell wall specifically interferes with biofilm formation. *Environmental microbiology reports*, (2015).
7. L. Duchesne, D. Gentili, M. Comes-Franchini, D. G. Fernig, Robust ligand shells for biological applications of gold nanoparticles. *Langmuir* **24**, 13572-13580 (2008).
8. J. R. Kremer, D. N. Mastronarde, J. R. McIntosh, Computer visualization of three-dimensional image data using IMOD. *Journal of structural biology* **116**, 71-76 (1996).
9. A. S. Frangakis, R. Hegerl, Noise reduction in electron tomographic reconstructions using nonlinear anisotropic diffusion. *Journal of structural biology* **135**, 239-250 (2001).
10. B. Langmead, S. L. Salzberg, Fast gapped-read alignment with Bowtie 2. *Nat Methods* **9**, 357-359 (2012).
11. S. Anders, P. T. Pyl, W. Huber, HTSeq-a Python framework to work with high-throughput sequencing data. *Bioinformatics* **31**, 166-169 (2015).
12. P. Nicolas *et al.*, Condition-dependent transcriptome reveals high-level regulatory architecture in Bacillus subtilis. *Science* **335**, 1103-1106 (2012).
13. R. H. Michna, B. Zhu, U. Mader, J. Stulke, SubtiWiki 2.0--an integrated database for the model organism Bacillus subtilis. *Nucleic acids research* **44**, D654-662 (2016).
14. G. A. O'Toole, Microtiter dish biofilm formation assay. *J Vis Exp*, (2011).
15. S. S. Branda, J. E. Gonzalez-Pastor, S. Ben-Yehuda, R. Losick, R. Kolter, Fruiting body formation by Bacillus subtilis. *Proc Natl Acad Sci U S A* **98**, 11621-11626 (2001).

Supporting Files:

Supporting File 1: Differentially expressed genes.

Supporting File 2: Differential expression by regulons.

Supporting File 3: TF categories by function.

Supporting Tables:

Supporting Table 1: Strains used in this study

Genotype	Reference
Bacillus subtilis NCIB 3610	(*15*)
ΔiolR (kan)	This work
ΔcueR (kan)	This work
ΔperR (kan)	This work
Pseudomonas aeruginosa PA14	Lab collection
Pseudomonas aeruginosa PA14, Ppuc-GFP (carb)	A kind gift from Ehud Banin

Supporting Table 2: Patient information

Patient	Medical Center	Gender	CFTR mutations
A4, H	Hadassa	F	W1282X
i	Hadassa	M	A455E
ii	Hadassah	M	G542X/F508
iii	Carmel	F	T360K, Q359K
iv	Hadassah	M	W1282X/W1282X
v	Haddasah	F	W1282X/F508
vi	Carmel	F	F508del